DOI: 10.13009/EUCASS2019-93

Wake Measurements of a MAV with Morphing Geometry

R. Bardera Mora, A. A. Rodríguez Sevillano**, A. García-Magariño*, E. Barroso Barderas**
** Instituto Nacional de Técnica Aeroespacial (INTA). Carretera de Ajalvir, km 4,5. 28850 Torrejón de Ardoz (MADRID), Spain.* barderar@inta.es, garciamga@inta.es barrosobe@inta.es
*** Escuela Técnica Superior de Ingeniería Aeronáutica y del Espacio*
Universidad Politécnica de Madrid.
Plaza del Cardenal Cisneros, 28040 Madrid, Spain. angel.rodriguez.sevillano@upm.es

Abstract
This research is focused on experimental and analytical methods of determining the aerodynamic forces acting on a micro air vehicle (MAV) with adaptive wing geometry (morphing geometry). The goal of this design is to modify the camber and thickness of its wings by using smart materials in order to achieve the optimum autonomy or range during the flight phases. Therefore, the most relevant morphing configurations have been studied. They were designed and manufactured at Technical University of Madrid (UPM) by means of additive manufacturing and tested in a low speed wind tunnel at National Institute of Aerospace Technology (INTA). Particle Image Velocimetry was used to study the wake structure of the different morphing configurations. The experimental tests were performed with a freestream velocity of 10 m/s for several angles of attack, from 0º to 30º. Two theoretical methods were applied: integral of transversal kinetic energy and Maskell's theory; for determining the induced drag coefficient and lift coefficient, respectively. A complete qualitative and quantitative study of the trailing vortex system behind the model is given in order to understand the aerodynamic behaviour of the morphing geometry.

1. Introduction

In last decades, the aerospace industry has developed a growing interest in Unmanned Aerial Vehicles (UAVs), a leading sector where taking innovation as primary factor, all types of vehicles with several geometries, propulsion systems and applications, can be designed. These vehicles have been designed for multiple missions where the human factor is not required. Therefore, in dangerous missions, unhealthy environments or inaccessible areas the human accidents can be avoided. The UAVs can be distinguished in different categories according to their performance characteristics. In this context, the relevant design parameters are weight, manufacturing costs and sizing. Mainly, the manufacturing costs have been the key point for that engineers and researchers could be focused on developing smaller vehicles in order to perform the unmanned activities. This group of smaller vehicles is known as Micro Aerial Vehicles (MAVs). Their main features are low aspect ratio (AR) and low range operation. Research centers and universities have been able to investigate new designs of MAVs due to their low manufacturing costs and small size. This is the case of aerodynamic challenges posed in the work of Moschetta [1]. The MAV designs taken into account the fixed wing, coaxial, biplane and the tilt-body concept. Marek [2] performed experimental tests to determine the aerodynamic coefficients in six different types of platform. The Zimmerman an elliptical platform resulted having the highest lift coefficient. Hence, Hassannalian and Abdelkefi [3] designed and manufactured a fixed wing MAV based on Zimmerman planform. Also, others authors (Flake and Standford) designed the Dragonfly MAV using Zimmerman planform. [4, 5].
Morphing geometry revolutionized the MAV design [6, 7, 8]. This configuration is based on adaptative wings to satisfy multiple roles with maximum aerodynamic efficiency. This concept is embraced into the category of biologically inspired MAVs. Morphing concept can be defined as the ability of an aircraft to adapt the geometry of its wings to each flight condition by optimizing the aerodynamic performance in each phase of the flight [9]. The morphing concept can be divided into the following categories [10]: planform alternation, out-of-plane transformation and airfoil profile adjustment. First category is based on modifications within the wing plane itself such as sweep angle, chord length or wingspan change. The second type of morphing is based on variations out of the wing plane such as wing twisting, span-wise bending or chord-wise bending. The airfoil profile adjustment is the interest category of this research. This type of morphing is based on camber airfoil change. Modify the camber of the

DOI: 10.13009/EUCASS2019-93

airfoil gives rise to a variation in the airfoil aerodynamic efficiency ($\frac{C_L}{C_D}$), zero-lift angle of attack (α), and also stall pattern [11]. Besides, the maximum lift coefficient increases with the maximum airfoil camber to chord ratio. Therefore, a MAV could flight at lower speed due to the achieved high lift coefficient by incrementing the camber of the airfoil. As consequence, high quality of capture video in real time would be achieved.

Generally, morphing concept is linked to smart materials. These materials present several advantages such as high energy density, high tolerance of strain, variable stiffness and ease of control. Therefore, these features have made them into new possibilities for developing morphing MAVs [13]. A MAV design with adaptative wings and Zimmerman planform has been designed by Barcala [14]. Piezoelectric materials, a type of smart materials, were used in order to modify the curvature of the wing depending on the flight conditions. These studies only provide the total aerodynamic coefficients. Consequently, this paper is focused on experimental study in the wake of the MAV model with morphing wings designed by Barcala [9, 12, 14]. The model is tested in two different configurations: unmodified configuration which is the MAV model at 0.0 V, and the configuration of maximum airfoil camber which is the MAV model at 5.0 V. Therefore, the main objective of this research is to obtain the components of drag: profile and induced drag components, and the lift coefficient. By integrating the theoretical formulation of Betz [15] and Maskell [16] at the wake region, the drag components can be determined. The experimental data is obtained by using an advanced non-intrusive technique, Particle Image Velocimetry (PIV).

2. MAV model

This paper is focused on aerodynamic performances of a MAV with an adaptative wing geometry or morphing MAV by wind tunnel testing. The main restriction of designing these type of vehicles is their low wing aspect ratio (LAR) besides of they perform at low Reynolds number. Although there is an aerodynamics investigation of MAVs with this flight regime developed by Pelletier and Muller [17] currently there is lack of knowledge which it requires aerodynamic studies for each new development of MAVs.

The geometry of the model is based on Zimmerman wing planform which consists of two half ellipses joined at $\frac{3}{4}$ and $\frac{1}{4}$ of the chord at wing root (see Figure 1). The MAV wing is designed with E61 (Eppler 61) airfoils and the fuselage with Whitcomb-il airfoils. The low aspect ratio (AR) is 2.5. This geometry was chosen in the preliminary design [9, 12, 14] according to the main aerodynamic parameters: minimum drag coefficient $C_{D,min}$, maximum lift coefficient $C_{L,max}$, and maximum lift to drag ratio $\left(\frac{C_L}{C_D}\right)_{max}$.

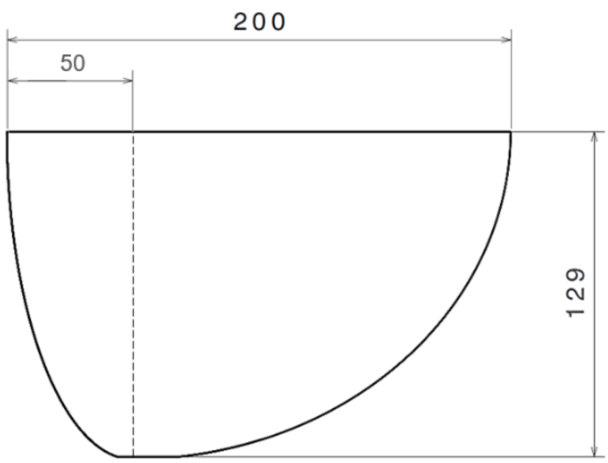

Figure 1: Dimensions of the Zimmerman wing.

Table 1 show the main design features of the morphing MAV [9, 12, 14]:

DOI: 10.13009/EUCASS2019-93

Table 1: Main design features of the MAV model.

Parameter	**Value**
Chord at the tip of the wing, c_t	0.025 m
Chord at wing root, c_r	0.200 m
Taper ratio, λ	0.124
Aspect ratio, AR	2.500
Wingspan, b	0.320 m
Mean aerodynamic chord	0.141 m
Mean geometry chord, CMG	0.127 m
Wing reference area, S	0.040 m^2
Dihedral angle	10º
Fuselage length, l	0.3 m
Fuselage width, d	0.06 m

Micro Fiber Composite (MFC) piezoelectric actuators are the smart material selected for obtaining the in-flight airfoil camber change. This material presents the ability of contracting and expanding depending of the applied voltage. The MFC actuators would be situated at 40% of the chord at wing root and at the lower surface of the wing. Previous studies of this MAV realized by Barcala [14] have carried out the variations of the airfoil curvature by using MFC actuators. The voltage intervals were between 0.0 V and 5.0 V. Figure 2 (left) shows the natural geometry Eppler 61 (E61) airfoil when no electric power was applied. On the other hand, the right image on Figure 2 corresponds to the maximum curvature of the Eppler 61 airfoil (cambered E61 airfoil), when the electric voltage applied was 5.0 V.

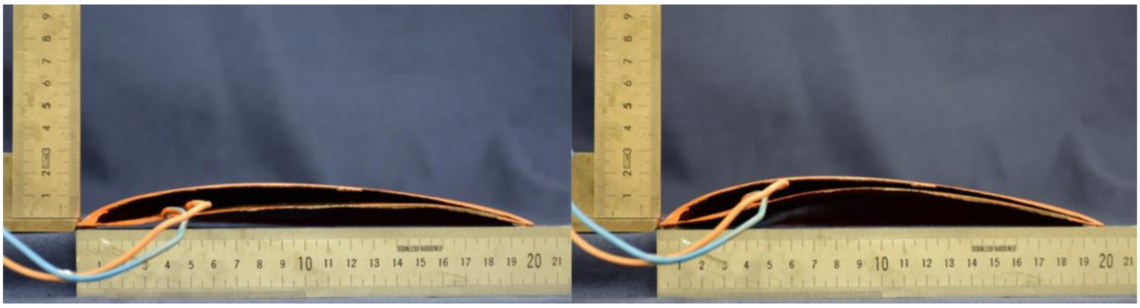

Figure 2: Natural geometry Eppler 61 airfoil (left) and cambered E61 airfoil (right).

The present research has not taken into account MFC actuators because the morphing MAV has been studied experimentally for determining the aerodynamic performances in the two different fixed configurations: the no-deformed E61 configuration which will be the model with no wing deformation and the modified E61 configuration which will be the model with the maximum curvature deformation. For observing the wing camber change, the front views of these two model are presented in Figure 3. Notice that the wing camber change it is not modifying the wingspan of the MAV model (*b=320mm*).

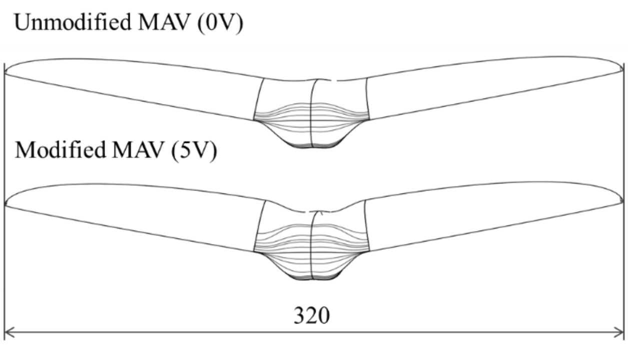

Figure 3: Front views of the two MAV configurations (Dimension in mm).

DOI: 10.13009/EUCASS2019-93

The MAV models were designed and manufactured at Technical University of Madrid (UPM) and they were tested at National Institute of Aerospace Technology (Instituto Nacional de Técnica Aeroespacial, INTA). The design was developed by using CATIA V5 and the manufacturing by means of 3D printing. Figure 4 shows the two MAV models.

Figure 4: No-deformed E61 configuration (White model) and modified E61 configuration (red model).

3. Experimental set-up and tests

The experimental tests were carried out in a Low Speed Wind Tunnel at National Institute of Aerospace Technology (INTA) in Madrid (Spain). This tunnel has a closed circuit with an elliptical open test section of 6 m^2. The DC engine, which is situated at the opposite side of the test section, works at 420 V allowing a maximum airflow speed of 60 m/s. This wind tunnel has a turbulence intensity lower than 0.5%.

Particle Image Velocimetry (PIV) was used for performing the experimental tests. PIV is an advanced experimental technique which has the advantage of measuring the velocity field in a non-intrusive manner. This technique measures the velocity of the flow by analyzing flow images pairs [18]. For achieving this, PIV requires tracer particles which have to be seeded in the airflow. Olive oil was chosen as for the generation of the tracer particles. A laser sheet have to be generated in order to go through the tracer particles and illuminate them. Two neodumium-doped yttrium aluminium garnet (Nd:YAG) lasers and an optical system was used for achieving this. The two lasers Nd:YAG have a laser pulse of 190 mJ within a time gap of 22 μs. The location of the tracer particles have to be recorded by a high resolution camera with 2048 x 2048 pixels (Nikon Nikkor 50 mm 1:1.4D). A cross-correlation implemented via Fast Fourier Transform (FFT) is carried out in order to obtain the average displacement of the tracer particles. The field of view (FOV) of the camera was $190\,x\,190\,mm^2$. The flow images are divided into interrogation window of 32 x 32 pixels. By using the Nyquist Sampling Criteria, these interrogation windows are overlapped by 50%. Moreover, the peak of correlation is adjusted to the subpixel accuracy based on the Gaussian theory. A final post-processing task to remove spurious data and fill the empty vectors is needed. Therefore, a local mean filter based on interrogation windows of 3 x 3 pixels has to be applied.

The MAV model in the two configurations previously explained (no-deformed E61 and deformed E61) were tested with a freestream velocity of the wind tunnel of 10 m/s, which results in a Reynolds number of 1.3×10^5 based on the chord at wing root ($c_r = 0.20\ m$). These two morphing configurations were performed at different angles of attack, from 0º to 30º with different intervals (0º, 5º, 10º, 15º, 20º, 25º, 26º, 27º and 30º). These values were chosen taking into account the stall condition. The experimental tests consisted in obtaining several transverse planes of the model at different planes downstream of the trailing edge of the model. The measurement planes were located at 1, 2, 3 and 4 chords (1c, 2c, 3c and 4c). A total of 36 planes were studied for each configuration of the model.

The experimental tests were performed using a full-scale model attached to a wood board by means of a streamlined support strut (see Figure 5). The half of the model was only studied due to its symmetry. Moreover, the model and the wood board had to be painted in black to avoid reflections of the laser plane. The CCD camera was located behind the model (Figure 5), parallel to the flow stream of the wind tunnel.

DOI: 10.13009/EUCASS2019-93

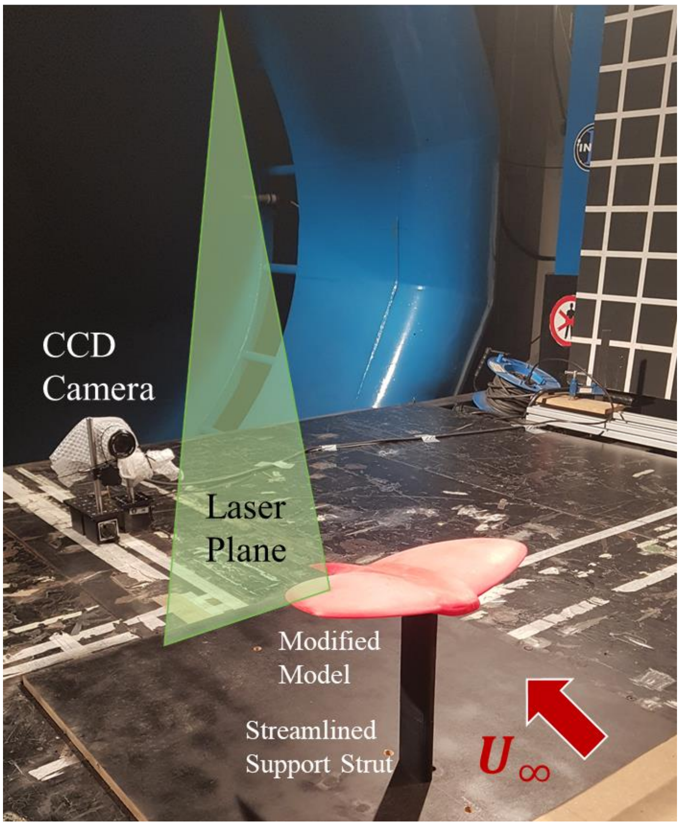

Figure 5: Experimental Set-up

4. Results

In this section, the results obtained from Particle Image Velocimetry technique will be presented. These results are presented in a qualitative and a quantitative form in order to analyse the flow structure of the wake with enough resolution. Therefore, the velocity and vorticity fields will be given in two-dimensional (2D) and three-dimensional (3D) graphs in order to obtain the visualization of the flow structure of the wake. Moreover, the aerodynamic performances will be presented in two-dimensional graphs.

4.1 Transversal Velocity Field

The visualization of the transversal velocity field was obtained at the transverse planes of the MAV model defined in the previous section. All transverse planes were located at different distances downstream of the trailing edge of the model. The chord at wing root ($c_r = 0.20\ m$) was chosen as the reference distance due to it is the biggest dimension chord of the wing. The transversal velocity field is given only in the more relevant cases.

The velocity magnitude V is defined as,

$$V = \sqrt{v^2 + w^2} \tag{1}$$

Where v and w are the velocity components in y-axis and z-axis directions, respectively.

Figure 6, 7 and 8 show the transversal velocity field of the two MAV configurations: no-deformed Eppler 61 and deformed Eppler 61 in different measurements planes and with different angles of attack. These results are presented in the classical PIV maps. The streamlines are plotted in order to localize the wing tip vortex. The same number of streamlines has been chosen to get a better understating of the aerodynamic behaviour of both configurations. The black triangle represents the reference point which is the tail of the model at 1 chord and with an angle of attack equal to 0º.

DOI: 10.13009/EUCASS2019-93

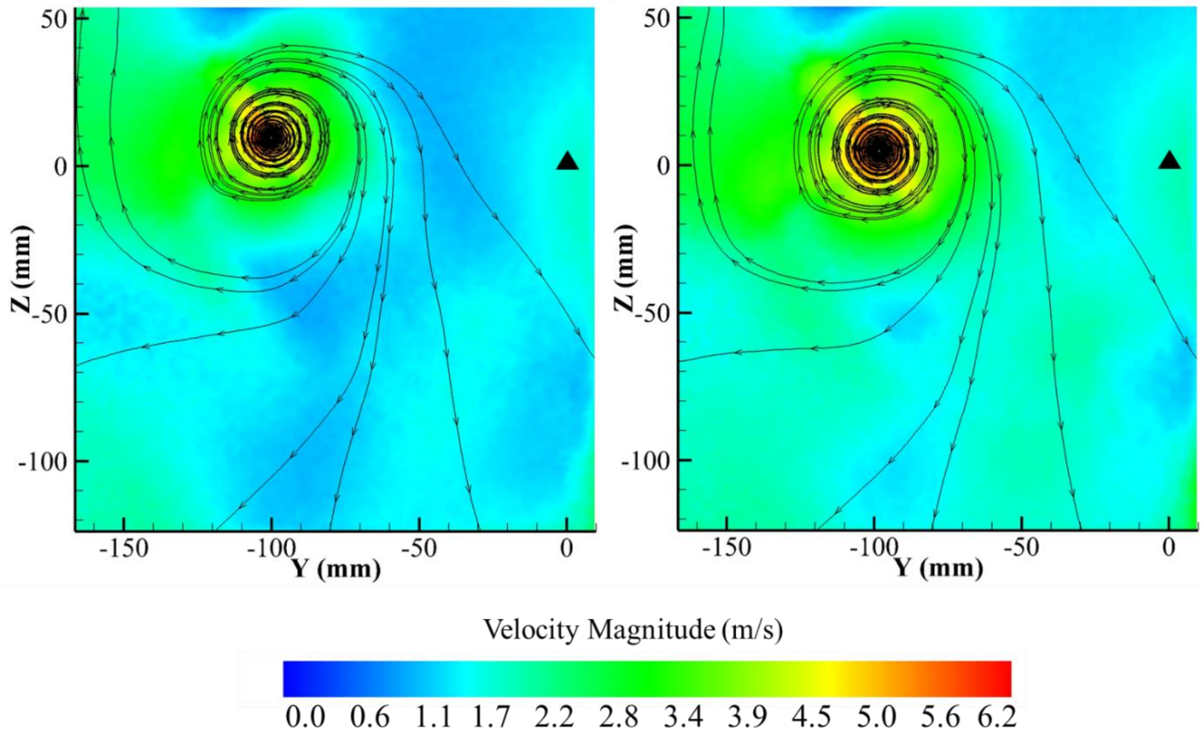

Figure 6: Velocity magnitude maps located at 2.0 chords downstream of the trailing edge of the model with an angle of attack of 5º. Natural geometry of Eppler 61 airfoil (left) and deformed geometry of Eppler 61 airfoil (right).

Figure 6 shows the velocity magnitude V maps located at 2 chords downstream on the trailing edge of the model with an angle of attack of 5º. The configuration of no-deformed E61 is on the left side of the Figure and the other configuration, deformed E61, is on the right side. In both configurations, the vortex formation at the tip of the wing (red region) can be seen. In that region the values of velocity are the highest. For no-deformed E61 configuration (left), the peak of maximum velocity is 6.20 m/s, and with the deformed E61, that peak of velocity is about 5.8 m/s. The diameter of the vortex seems to be greater with the deformed E61 configuration due to the red region is bigger too. Outside of the vortex core, the velocity with the no-deformed configuration is lower than with the deformed configuration. The vortex core is upper the reference point in both configurations.

Figure 7 and 8 show the velocity magnitude V maps located at 2 and 3 chords downstream on the trailing edge of the model with an angle of attack of 27º and 30º, respectively. In both Figures, the no-deformed E61 configuration can be seen on the left side, and the deformed E61 configuration can be seen on the right side.

In Figure 7, there is clearly a significance difference between the two configurations. Near the region of the vortex, the velocity magnitude is up to 4.5 m/s (green region) with the no-deformed E61 configuration. However, that velocity magnitude reaches up to 8.5 m/s (red region) with the deformed E61 configuration. Besides, with the no-deformed E61 configuration, there is a blue region with a wide size about 60 mm which has very low velocity, less than 1.5 m/s. However, that same region in the other configuration (deformed E61) has values of the velocity magnitude up to 8.5 m/s. As due to near the vortex core (vortex core has been defined as the maximum peak of axial vorticity; it will be detailed in the non-dimensional axial vorticity maps in section 4.2) the velocities with the deformed configuration are much higher than with the no-deformed configuration, the structure of the vortex presents higher intensity and also it could be more stable. In fact it could be possible that the flow of the no-deformed E61 configuration was started to become detached.
In this case (and in both configurations), the vortex core has been displaced below the reference point. Also, the vortex core is moving in wingspan direction to the opposite side of the tail (reference point) as the distance of the planes (2c and 3c) is increasing.

DOI: 10.13009/EUCASS2019-93

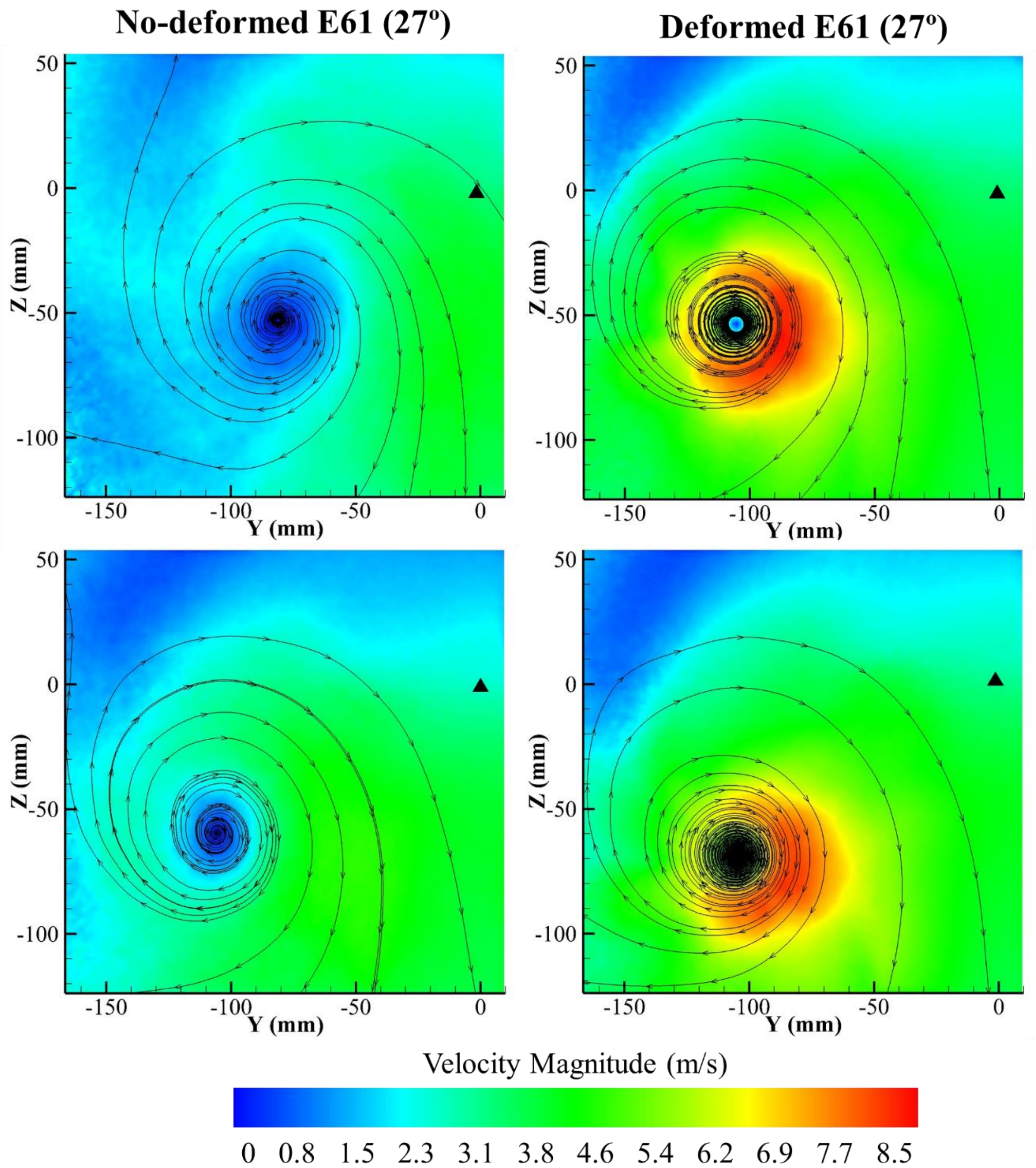

Figure 7: Velocity Magnitude maps at 2c (upper maps) and at 3c (lower maps). No-deformed E61 (left) and deformed E61 (right) with an angle of attack of 27º.

The transversal velocity fields showed in Figure 8 have roughly a similar behaviour in both configurations. Although the streamlines show clearly the rotation of the flow, the flow could be detached because the velocities are very low. The velocity values do not exceed 5 m/s in both configurations.

DOI: 10.13009/EUCASS2019-93

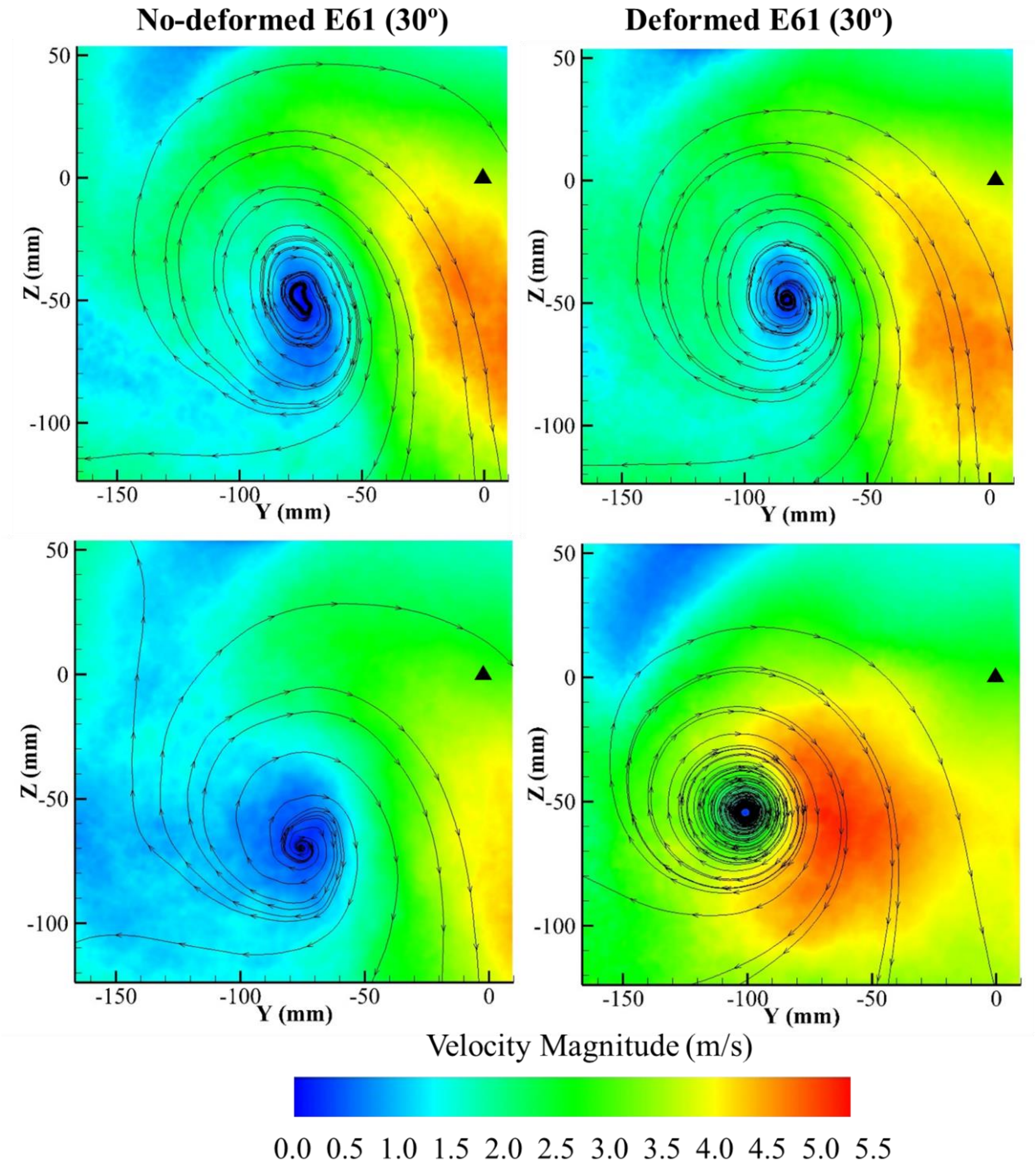

Figure 8: Velocity Magnitude maps at 2c (upper maps) and at 3c (lower maps). No-deformed E61 (left) and deformed E61 (right) with an angle of attack of 30º.

The structure of the vortex generated by the wing tip in three-dimensional can be observed in Figure 9. The 3D maps are presented for the measurement plane at 2 chords and for angles of attack: 20º, 25º, 27º and 30º. All of them show the vortex formation which consists of a region in where the velocity magnitude reaches its maximum value (red region). In the middle of that region of maximum velocity, there is a minimum peak of velocity (blue region) which represents the center of the vortex.

The velocity magnitude is increasing as the angle of attack increases until obtaining the maximum value for an angle of attack of 15º in both configurations. From that angle of attack on, the velocity magnitude starts decreasing. Moreover, in all cases the velocity magnitude in deformed E61 configuration is always greater than in the no-deformed E61 configuration. Thus, for an angle of attack of 20º, the maximum velocity magnitude is 11 m/s with de deformed configuration and 9 m/s with the no-deformed configuration. The rest of the values are presented in the Table 2:

DOI: 10.13009/EUCASS2019-93

Table 2: Velocity Magnitude, V

Angle of attack, α	MAV configuration	V
$\alpha = 25°$	No-deformed E61 configuration	6.5 m/s
	Deformed E61 configuration	8.60 m/s
$\alpha = 27°$	No-deformed E61 configuration	4 m/s
	Deformed E61 configuration	8 m/s
$\alpha = 30°$	No-deformed E61 configuration	4 m/s.
	Deformed E61 configuration	5 m/s

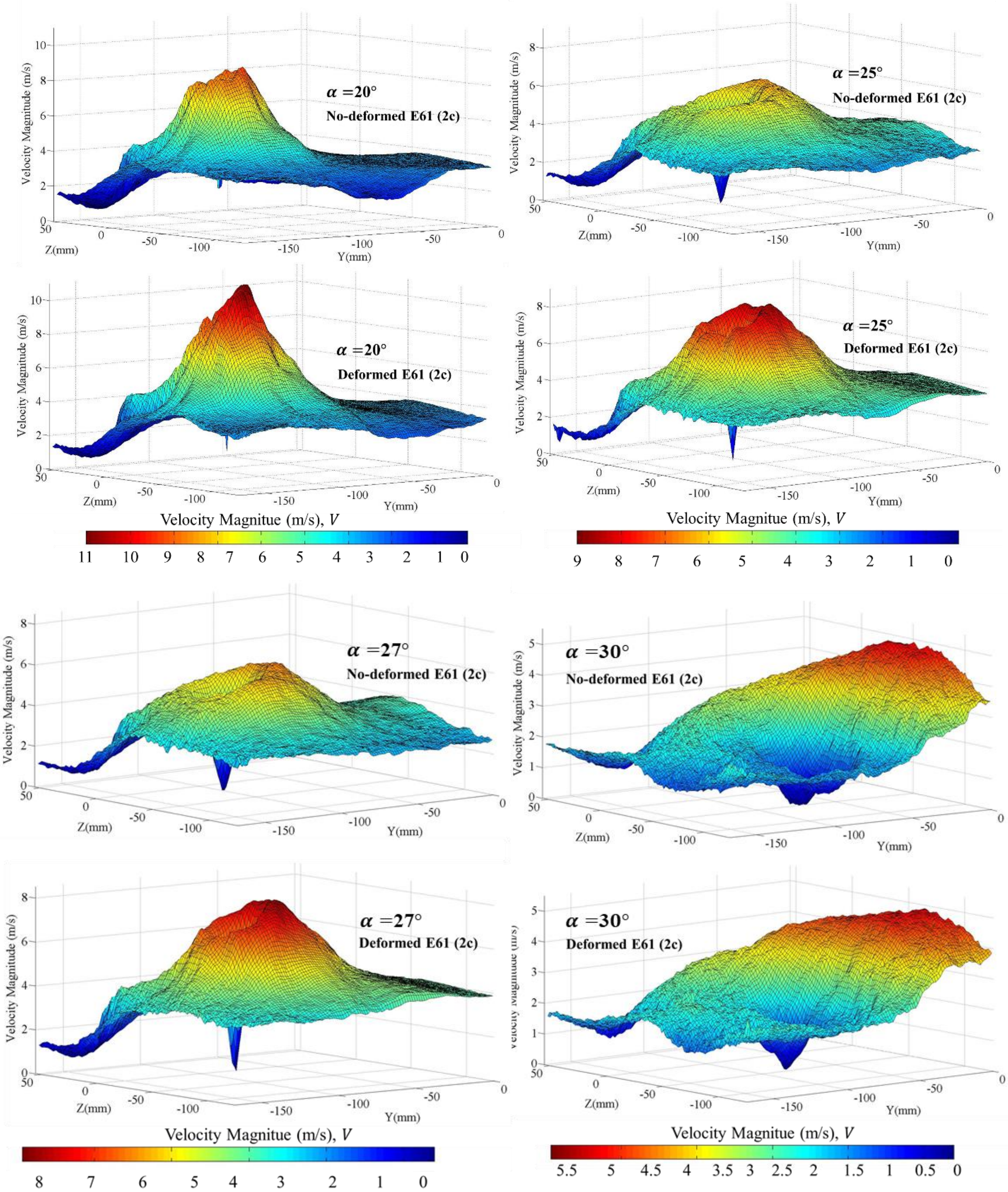

Figure 9: 3D Velocity Magnitude maps at 2 chords (2c) with an angle of attack of 20º, 25º, 27º and 30º.

DOI: 10.13009/EUCASS2019-93

4.2 Induced Drag Coefficient

The induced drag coefficient has been obtained from the experimental data of the velocity transversal fields. A theoretical method based on the integral of the transversal kinetic energy [19] has been chosen for determining the induced drag component. This method is only for studying the flow in the wake at planes which are enough downstream of the trailing edge of the model (Trefftz's Plane). Equation (2) defines the induced drag coefficient, C_{Di},

$$C_{Di} = \frac{1}{A}\iint_W \left(\frac{v^2}{U_\infty^2} + \frac{w^2}{U_\infty^2}\right) dydz \tag{2}$$

Where, A is the reference area and U_∞ is the freestream velocity.

By discretizing the equation (2),

$$C_{Di} = \frac{1}{A}\sum\sum\left(\frac{v^2}{U_\infty^2} + \frac{w^2}{U_\infty^2}\right) \Delta y \Delta z \tag{3}$$

Where $\Delta y, \Delta y$ are the window size in the flow ($\Delta y = \Delta y = 1.53\ mm$).

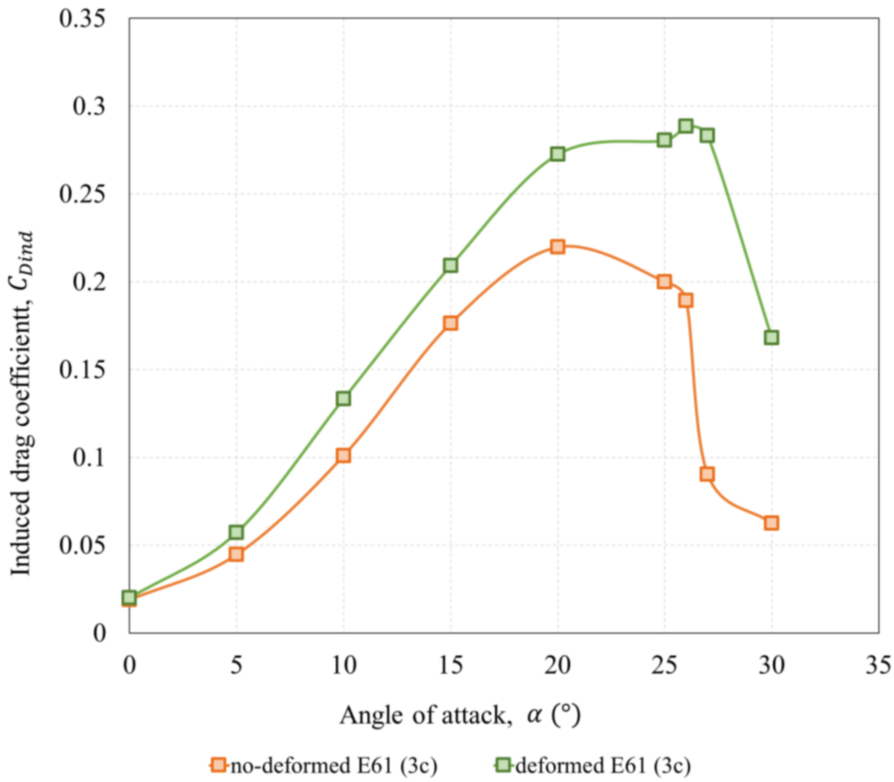

Figure 10: Curve of induced drag coefficient C_{Dind} vs. angle of attack α, for the MAV model in the two configurations (no-deformed E61 and deformed E61) at 3 chords (3c).

The values of induced drag coefficient depending on the angle of attack are plotted in the Figure 10. Only the induced drag coefficients obtained in the measurement plane at 3 chords downstream of the trailing edge of the model are represented in the Figure 10 because the values obtained in the rest of the measurement planes (1c, 2c and 4c) are roughly similar.

The induced drag coefficient is the same ($C_{Dind} = 0.02$) in both configurations (no-deformed E61 and deformed E61) at the angle of attack of 0º. The no-deformed E61 configuration show lower values of induced drag in all angles of attack. The maximum value of this aerodynamic parameter is 0.22 ($C_{Dind} = 0.22$) whit an angle of attack of 20º. However, in the deformed E61 configuration, the maximum value of C_{Dind} is 0.29 and with an angle of attack of 26º.

DOI: 10.13009/EUCASS2019-93

4.2 Vorticity Field

The vorticity field was obtained in the same measurement planes than the velocity transversal field, at 1c, 2c, 3c and 4c and also for all angles of attack (from 0º to 30º). This variable has been obtained from the velocity data since it only depends on the velocity spatial derivatives. Therefore, the axial vorticity ξ is defined as in equation (4):

$$\xi = \frac{\partial w}{\partial y} - \frac{\partial v}{\partial z} = (\nabla \times \vec{V}) \cdot \vec{\imath} \tag{4}$$

Where ∇ is the Hamilton differential operator defined as in the following expression (5):

$$\nabla = \left(\frac{\partial}{\partial x}, \frac{\partial}{\partial y}, \frac{\partial}{\partial z}\right) \tag{5}$$

The vorticity field results are presented in non-dimensional form. Thus, the non-dimensional axial vorticity $\tilde{\xi}$ is defined as in the expression (6):

$$\tilde{\xi} = \frac{\left(\frac{b}{2}\right) \cdot \xi}{U_\infty} \tag{6}$$

Where b is the wingspan (*b=320 mm*).

In Figure 11, the non-dimensional axial vorticity is presented for the no-deformed configuration (left) and for the deformed configuration (right) in the measurement plane located at 2.0 chords downstream of the trailing edge of the model and for the angle of attack of 5º. The maximum peak of axil vorticity takes place in the center of the vortex (vortex core). The value of maximum vorticity is -100 (blue region) for the no-deformed configuration and -73 (green region) for the deformed configuration. Besides, the center of the vortex with the no-deformed configuration is placed in a higher position with respect to the tail (reference point) than the deformed configuration (the reference point is the tail of the model at 1c and for the angle of attack of 0º and it is represented by the dotted black line).

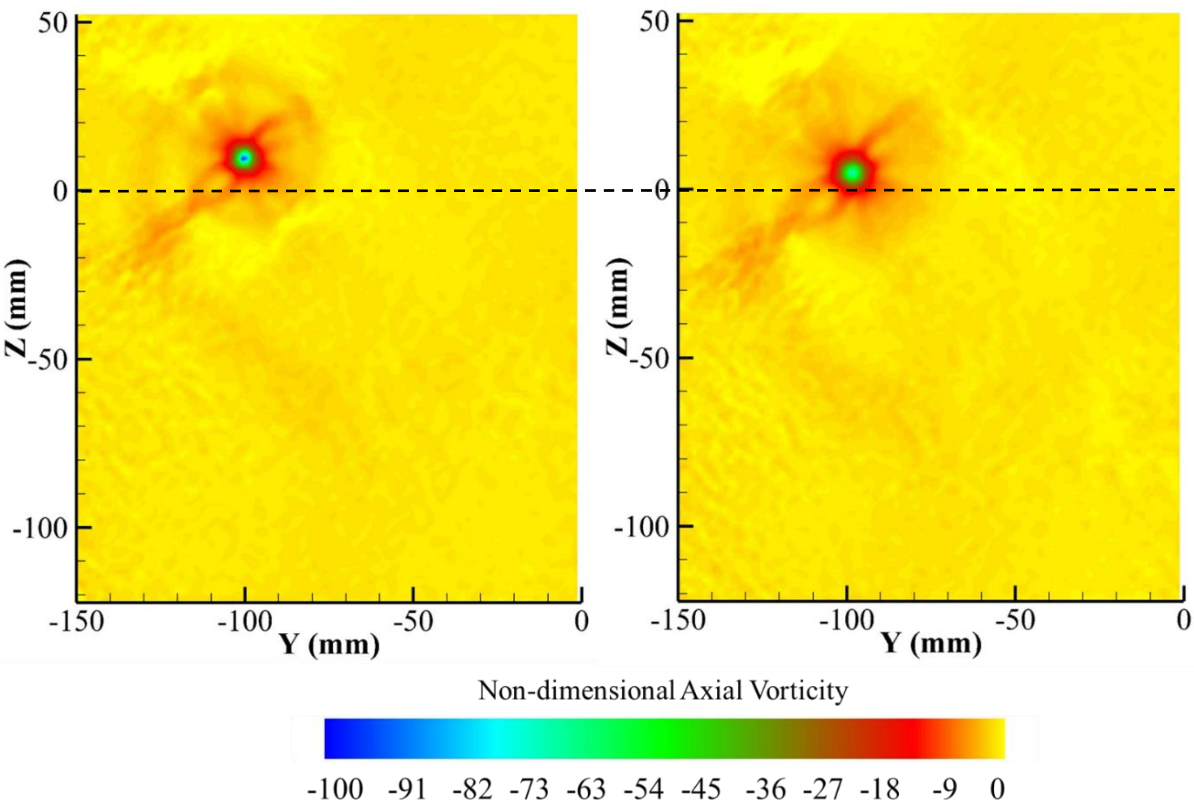

Figure 11: Non-dimensional axial vorticity maps located at 2.0 chords downstream of the trailing edge of the model with an angle of attack of 5º. Natural geometry of Eppler 61 airfoil (left) and deformed geometry of Eppler 61 airfoil (right).

DOI: 10.13009/EUCASS2019-93

Figure 12 shows the non-dimensional axial vorticity in three-dimensional to analyse with more detail the structure of the vortex. The results are presented for the same measurement planes and same angles of attack than the 3D velocity results (2c for α =20º, 25º, 27º and 30º). In Figure 12 can be seen clearly the vortex core which has been defined as the peak of maximum vorticity. For the angles of attack lower than 20º ($\alpha <$ 20º), the axial vorticity in the no-deformed E61 configuration is higher than the deformed configuration. However, from α =20º on, ($\alpha \geq$ 20º), the axial vorticity in the no-deformed E61 configuration is lower than the other configuration. The values of the maximum non-dimensional axial vorticity $\tilde{\xi}_{max}$ are given in the following table (Table

Table 3: Maximum non-dimensional axial vorticity $\tilde{\xi}_{max}$

Angle of attack, α	MAV configuration	$\tilde{\xi}_{max}$
$\alpha = 20°$	No-deformed E61 configuration	-59.00
	Deformed E61 configuration	-70.00
$\alpha = 25°$	No-deformed E61 configuration	-13.40
	Deformed E61 configuration	-25.00
$\alpha = 27°$	No-deformed E61 configuration	-12.40
	Deformed E61 configuration	-21.65
$\alpha = 30°$	No-deformed E61 configuration	-4.68
	Deformed E61 configuration	-4.70

In both configurations (no-deformed and deformed) the non-dimensional axial vorticity maintain the same form as in the case for α =20º. The survey wake region shows that there is no axial vorticity outside of the wake of the model. Therefore, the axial vorticity is concentrated only in a small region which represents the maximum peak in the 3D graphs of the Figure 9. For the no-deformed E61 configuration, that peak of axial vorticity has been notably reduced for the angles of attack of 25º and 27º. This represents the beginning of the stall condition. However, with the deformed E61 configuration, the flow is still attached at α = 25°. Although, the peak of maximum vorticity is reduced, the axial vorticity has the same trend as in the previous angles of attack. The beginning of the stall condition for the deformed E61 configuration would be from α = 27° on. In both configurations, the flow is totally detached (stall totally developed) for the angle of attack of 30º because the graphs show that there is no peak of maximum vorticity.

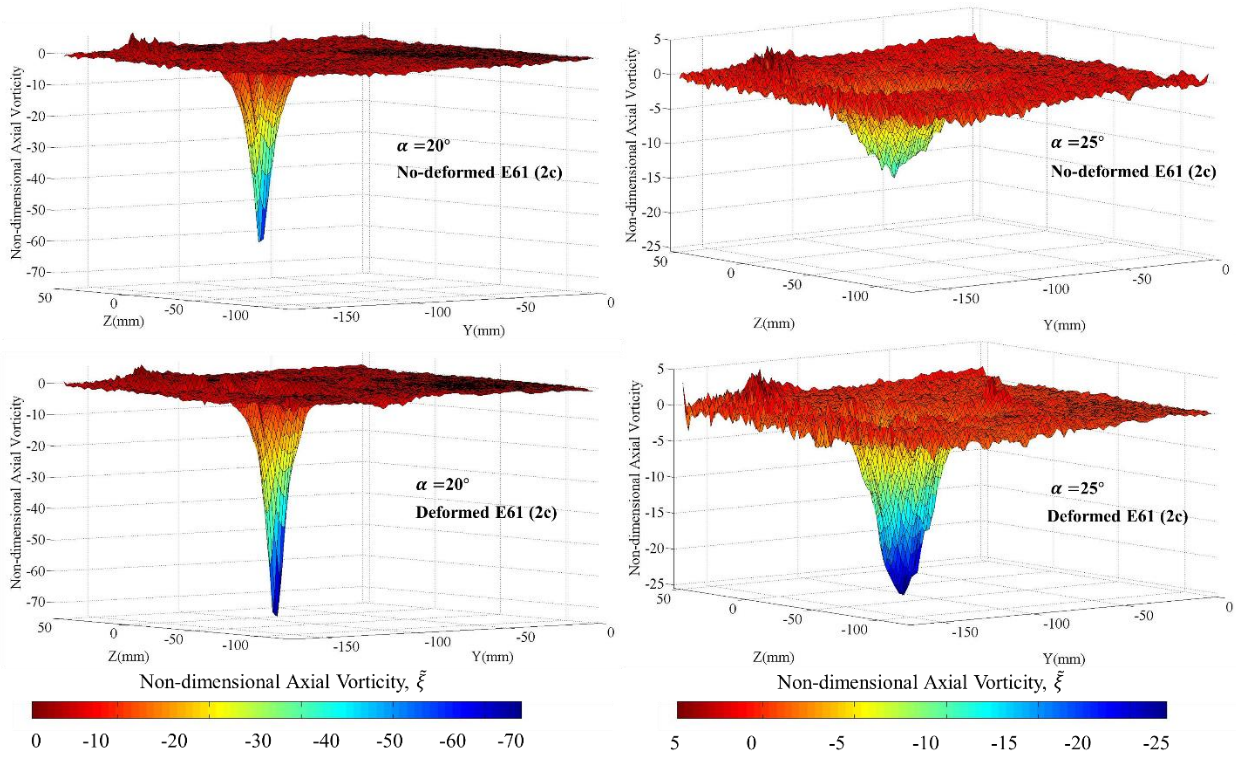

DOI: 10.13009/EUCASS2019-93

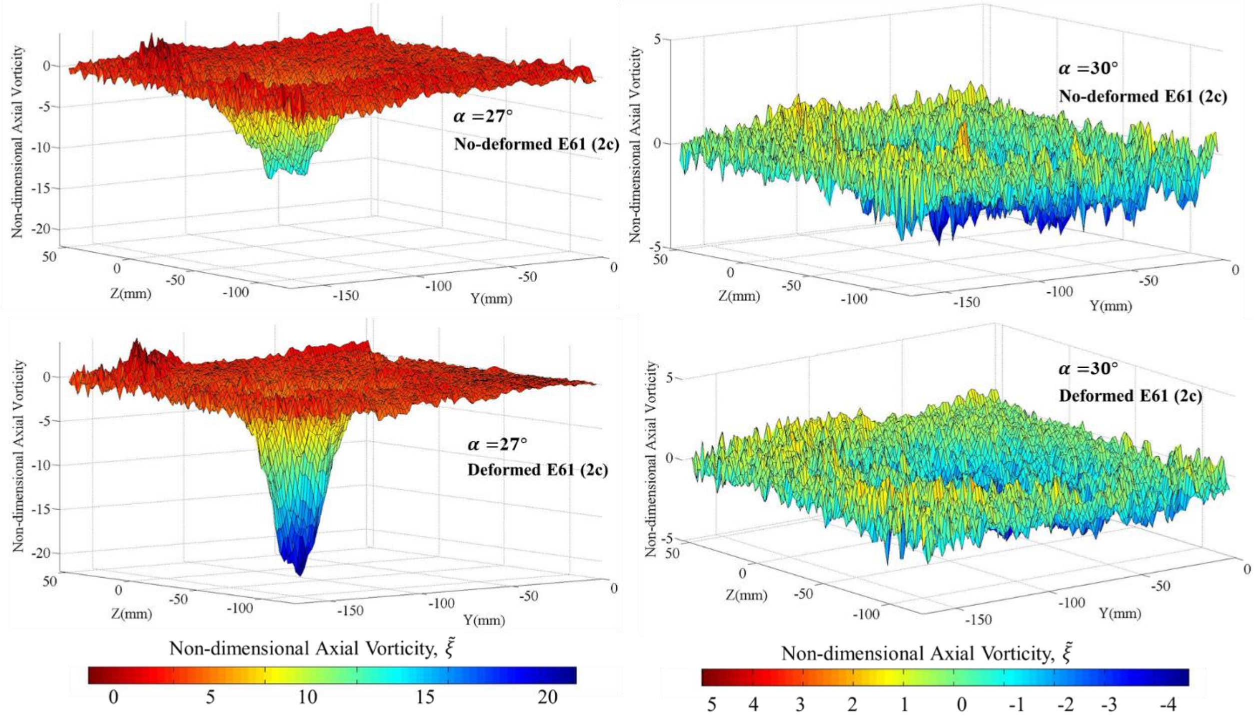

Figure 12: Non-dimensional axial vorticity maps located at 2.0 chords downstream of the trailing edge of the model with an angle of attack of 20º, 25º, 27º and 30º.

3.4 Lift Coefficient

The lift coefficient has been obtained from the experimental data of the axial vorticity field. As with the induced drag component, the determination of the lift coefficient has been realized by using a theoretical method based on Maskell's theory [20]. This method is only for studying the flow in the wake at planes which are enough downstream of the trailing edge of the model (Treffz's Plane). The lift coefficient is defined as in equation (7):

$$C_L = \frac{2}{U_\infty A}\iint_W y\xi dydz = \frac{2}{U_\infty A}\sum\sum y \cdot \xi(y,z)\ \Delta y \Delta z \qquad (7)$$

In Figure 13, the curve of lift coefficient depending on the angle of attack α is plotted. This graph has been obtained only for the measurement plane at 3 chords downstream on the trailing edge of the model because in the measurement planes at 2 chords and 4 chords the values of the lift coefficient maintain the same trend as this one. Although, in the measurement plane at 1 chord the flow is not completed uniform, the lift coefficient also keep the trend in the majority of the points.

The graph (Figure 13) shows the typical linear segment slope in which the lift coefficient C_L is increasing as the angle of attack α is getting bigger. This linear segment will be finished at a certain point in which the lift will start decreasing known as the stall condition. That certain point is the critical angle of attack α_c in which the lift coefficient reaches the maximum value, C_{Lmax}.

At this point, the maximum lift coefficient is 1.31 for the no-deformed E61 configuration and its corresponding angle of attack is 25º. However, the maximum lift coefficient for the deformed E61 configuration is achieved for a higher angle of attack, 27º. The value of maximum lift coefficient is also higher and it is 1.50. From these critical angles of attack on the stall condition will start for the MAV model ($\alpha_c = 25$º for no-deformed E61 configuration and $\alpha_c = 27$º for deformed E61 configuration).

Notice that the lift coefficients for the deformed E61 are higher than the no-deformed E61 for all angles of attack except for the angle of attack equal to 0º, in which the value is 0.2 for the two configurations.

Moreover, it is important taking into account that the stall condition has been obtained based on experimental data and for certain angles of attack. Therefore, the stall condition for the no-deformed E61 configuration would be for $\alpha_c = 25$º but for the deformed E61 configuration would be between $\alpha_c = 27$º and $\alpha_c = 30$º due to the 3D axial vorticity maps.

DOI: 10.13009/EUCASS2019-93

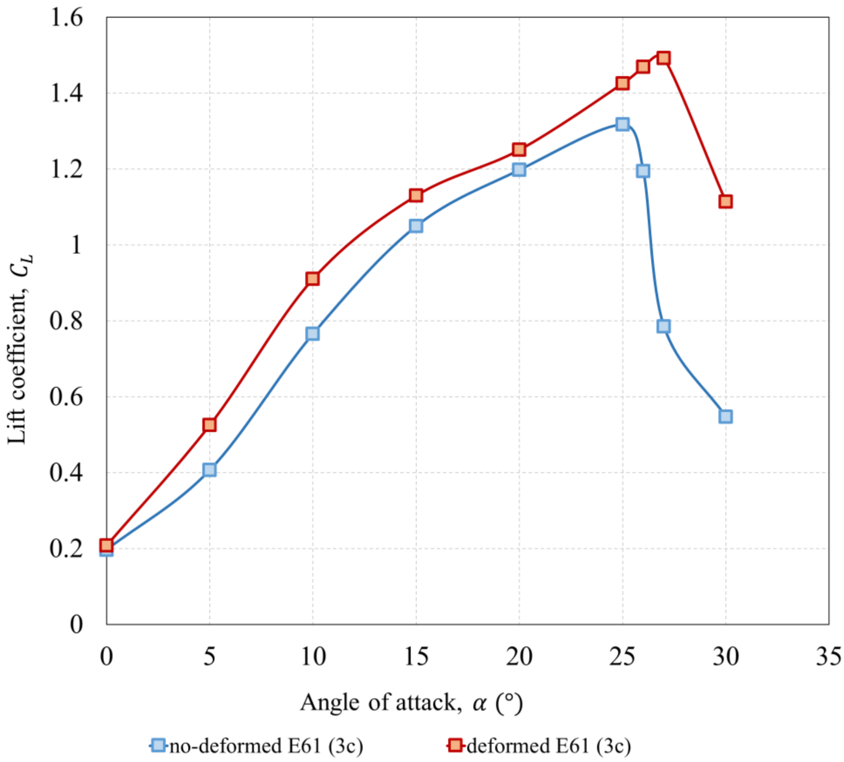

Figure 13: Curve of lift coefficient C_L vs. angle of attack α, for the MAV model in the two configurations (no-deformed E61 and deformed E61) at 3 chords (3c).

5. Conclusions

This study has been focused on obtaining the aerodynamic forces of a Micro Aerial Vehicle (MAV) whit morphing geometry. This model has been investigated in two configurations: the no-deformed E61 airfoil which is the configuration with no wind deformation (no electric power) and the deformed E61 configuration which corresponds to the maximum curvature deformation (5.0V). These model were designed and manufactured at Technical University of Madrid (UPM) by using 3D printing and they were tested in a low speed wind tunnel at National Institute of Aerospace Technology (INTA) facilities. Particle Image Velocimetry was used to obtain the velocity and vorticity field.

The experimental tests were performed with a freestream velocity of 10 m/s for several angles of attack, from 0º to 30º. The curves of induced drag coefficient and lift coefficient vs α were obtained by using theoretical methods based on the wake survey (Treffz's Plane). From the lift coefficient slope, the stall angle of attack for the no-deformed E61 configuration has resulted to be 25º ($\alpha_c = 25$º). For the angle of attack, the maximum lift coefficient is 1.31 ($C_{Lmax} = 1.31$). However, for the deformed E61 configuration, the stall angle has been 27º ($\alpha_c = 27$º) and the maximum lift 1.50 ($C_{Lmax} = 1.50$). Taking into account the 3D axial vorticity, the stall condition for the deformed E61 configuration would be from $\alpha = 27$º to $\alpha = 30$º. Therefore, the deformed E61 configuration is more efficient than the no-deformed E61 configuration due to the maximum lift coefficient is higher in all angles of attack and also the stall condition is delayed, from 25º to 27º.

DOI: 10.13009/EUCASS2019-93

References

[1]Moschetta, J. L. "The aerodynamics of micro air cehicle: technical challeges and scientific issues," *International Journal of Engineering Systems Modelling and Simulation*, Vol. 6, No. 3/4, 2014, pp. 134-148. ISSN 1755-9758.

[2] Marek, P. L., "Design, optimization and flight testing of a micro air vehicle" Doctoral dissertation, University of Glasgow, 2008.

[3] Hassanalian, M., and Abdelkefi, A., "Design and manufacture of a fixed wing MAV with Zimmerman planform" *AIAA SciTech, 54th AIAA Aerospace Sciences Meeting*, January 2016. AIAA 2016-1743.

[4] Stanford, B., Sytsma, M., Albertani, R., Viieru, D., Shyy, W., and Ifju, P., "Static Aeroelastic Model Validation of Membrane Micro Air Vehicle Wings", *AIAA Journal*, Vol. 45, No. 12, 2007, pp. 2828-2837.

[5] Flake, J., Frischknecht, B., Hansen, S., Knoebel, N., Ostler, J., &Tuley, B., "Development of the Stableyes Unmanned Air Vehicle", *8th International Micro Air Vehicle Competition*, The University of Arizona, Tucson, AZ, 2004, pp. 1-10.

[6] Silvestro Barbarino, Onur Bilgen, Rafic M. Ajaj, Michael I. Friswell, and Daniel J. Inman. "A Review of Morphing Aircraft" *Journal Of Intelligent Material Systems And Structures*, Vol. 22—June 2011 pp 823-877 DOI: 10.1177/1045389x11414084.

[7] Zheng Min , Vu Khac Kien & Liew J.Y. Richard (2010) ''Aircraft morphing wing concepts with radical geometry change'', The *IES Journal Part A: Civil & Structural Engineering*, 3:3, 188-195, DOI: 10.1080/19373261003607972

[8] De Breuker R, Abdalla MM and Gürdal Z ''A generic morphing wing analysis and design framework''. *Journal of Intelligent Material Systems and Structures*, 2010, 22(10): 1025-1039

[9] Barcala-Montejano, M. A., Rodríguez-Sevillano, A., Crespo-Moreno, J., Bardera Mora, R., and Silva-González, A. J. "Optimized performance of a morphing micro air vehicle." Unmanned Aircraft Systems (ICUAS), 2015 International Conference pp. 794-800. IEEE Journal of Intelligent Material Systems and Structures.

[10] A,Y,N, Sofla, S,A, Meguid, K,T, Tan, W,K, Yeo ''Shape morphing of aircraft wing: Status and Challenges''. Materiald and Design, 2010.

[11] Gen MS, Özkan G, Özden M, et al ''Interaction of tip vortex and laminar separation bubble over wings with different aspect ratios under low Reynolds numbers'' Proceedings of the Institution of Mechanical Engineers, Part C: Journal of Mechanical Engineering Science. Epub ahead of print 3 January. DOI: 10. 1177/0954406217749270.

[12] Barcala-Montejano, M. A., Rodríguez-Sevillano, A., Bardera-Mora, R., García-Ramirez, J., Leon-Calero, M., and Nova-Trigueros, J. "Development of a morphing wing in a micro air vehicle" *SMART* 2017.

[13] Jian Sun, Qinghua Guan and Qinghua Guan, "Morphing aircraft based on smart materials and structures: A state-of-the-art review" Intelligent Material Systems and Structures, 27(17), 2016, pp 2289–2312. DOI:10.1177/1045389X16629569.

[14] Barcala-Montejano, M. A., Rodríguez-Sevillano, J., Bardera Mora, R., "Smart materials applied in a micro remotely piloted aircraft system with morphing wing'' *Journal of Intelligent Material Systems and Structures*, 2018.

[15] Betz, A."A Method for the Direct Determination of Profile Drag" Zeitschrift für Flugtechnik und Motorluftschiffahrt, Vol. 16, 1925, pp.42-44.

[16] Maskell, E.C., ''Progress Towards a Method for the Measurement of the Components of the Drag of a Wing of Finite Span,''RAE Technical Report 72232, 1972.

[17] Pelletier A and Mueller TJ ''Low Reynolds number aerodynamics of low-aspect-ratio, thin/flat/cambered-plate wings''. *Journal of Aircraft 37(5):* 825-832.

[18] A. K. Prasad, "Particle image velocimetry," Current Science, vol. 79, no. 1, pp. 51–60, 2000.

[19] Amant, S., ''Drag prediction and decomposition, from wake surveys and calculations, in subsonic flows'' AIAA 2001-2446, June 2001.

[20] Brune, G.W., "'Quantitative Three-Dimensional Low-Speed Wake Surveys'' Boeing Commercial Airplane Group Seattle, Washington, 1991.